Electric field tuning of the optical absorbance of topological insulator thin films

Hadi Khanjani and MirFaez Miri ●*

Department of Physics, University of Tehran, P. O. Box 14395-547, Tehran, Iran

In view of electro-optic modulators and switches operating in the terahertz frequency range, we study the absorbance of a topological insulator (TI) thin film subjected to a static electric field. Adopting the Hamiltonian for the three-dimensional Bi_2Se_3 class of TIs including terms to second order in the electron wave vector and to first order in the electric field, we present an effective model for a TI thin film. We demonstrate the distinct influences of in-plane and out-of-plane external electric fields, the in-plane electric field-induced dichroism, and the electric field and chemical potential tuning of the absorbance edge. Under the influence of an out-of-plane electric field, a TI film with a thickness of about 2 nm exhibits a considerable absorbance at the absorbance edge. Of prime practical importance, the absorbance edge can be shifted about 0.3 eV with the application of moderate electric fields about 0.4 Vnm^{-1} or with chemical potential variations about 0.3 eV.

I. INTRODUCTION

Optical modulators are of paramount importance in photonics and optoelectronics [1,2]. Based on their principle of operation, optical modulators can be categorized as all-optical, electro-optic, magneto-optic, or acousto-optic modulators, and so on. Electro-optic modulators can be further classified as electro-refractive modulators or *electro-absorptive modulators*. To realize electro-absorptive modulators, intriguing effects such as electro-absorption, saturable absorption, the Franz-Keldysh effect, and the quantum-confined Stark effect are exploited. The discovery of graphene has opened a new chapter of optoelectronics [3]. Particularly, graphene has been recognized as a promising material for optical modulators [4,5]. Indeed, across the whole infrared to visible spectral range, a monolayer graphene exhibits an absorbance $\pi\alpha_{\text{fine}} \approx 2.3\%$ [6,7]—expressed in terms of the fine-structure constant α_{fine}—which is two orders of magnitude larger than the absorbance of a conventional photodetector material $Hg_{1-x}Cd_xTe$ of the same thickness [8]. Transition-metal dichalcogenides and black phosphorus have also gained attention. Thinned to monolayers, transition-metal dichalcogenides such as MoS_2, $MoSe_2$, WS_2, and WSe_2 exhibit a direct band gap ranging from 1.57 to 2 eV. Having a band gap ranging from 0.3 to 1.5 eV, monolayer and few-layer phosphorene offer optical properties complementary to graphene and transition-metal dichalcogenides [4,5]. In this respect, topological insulator (TI) thin films with an absorbance $\frac{\pi}{2}\alpha_{\text{fine}} \approx 1.1\%$ for photon energies below 0.3 eV deserve particular attention [9].

Three-dimensional TIs, such as bismuth chalcogenide materials Bi_2Se_3 and Bi_2Te_3, are a class of band insulators characterized by insulating bulk and conducting surface states robust with respect to perturbations that obey time-reversal symmetry [10,11]. Ideally, the surface states can be described by a two-dimensional Dirac-like Hamiltonian. These bismuth chalcogenides are layered materials with van der Waals bonded quintuple layers (QLs). By means of epitaxial methods, vapor-solid growth, and mechanical exfoliation, TI thin films with thicknesses down to 1 QL $\approx$ 1 nm have been fabricated [12–14]. A surface of a TI film hosts one single gapless Dirac cone [15–18]. The surface-state decay length into the bulk l_s, is an important characteristic length. Indeed, in TI thin films, the top and bottom surface states hybridize with each other when the thickness becomes comparable to l_s and, subsequently, a thickness-dependent energy gap at the Dirac point appears [19,20]. Using angle-resolved photoemission spectroscopy, the band structure of molecular beam epitaxy grown Bi_2Se_3 film with a thickness from 1 to 50 QL is studied. The energy gap opening is observed when the thickness is below 6 QL [19]. The hybridization of surface states is at the origin of the appealing properties of TI thin films [21–31]. In particular, *electric field tuning* of the surface band structure of TI thin films is experimentally demonstrated [24].

TI thin films are introduced as an excellent platform for terahertz and infrared detectors [9,29,32,33]. To take into account the intersurface coupling and the inversion symmetry breaking via an external electric field perpendicular to the film, an effective Hamiltonian including terms to first order in the electron wave vector is adopted [32]. But, according to this Hamiltonian, the electric field does not influence the energy band gap. In this framework, only the film thickness can be altered to roughly tune the detector. A more sophisticated Hamiltonian including quadratic terms in the electron wave vector is utilized to confirm that the band gap can be tuned with the application of modest electric fields about 0.3 Vnm^{-1}, in agreement with first-principles calculations based on the density functional theory [33].

In view of electro-absorptive modulators and switches operating in the terahertz frequency range, we revisit the absorbance of the Bi_2Se_3 class of TI thin films. We follow Shan

*mirfaez_miri@ut.ac.ir

et al. [20] to establish an effective model for a TI thin film, starting from the electronic model for *bulk* material. We adopt the Hamiltonian for the bulk TI, including all symmetry-allowed terms to second order in the electron wave vector and to first order in the external electric field, presented by Brems *et al.* [34]. To emphasize the significance of the hybridization phenomenon, we study 6 QL and thinner films. We demonstrate the frequency dependence of the absorbance, the distinct influences of in-plane and out-of-plane external electric fields, the in-plane electric field-induced dichroism, the electric field and chemical potential tuning of the absorbance edge, and the impact of the electron-hole asymmetry on the absorbance edge. The maximum absorbance of a 6 QL film is 1.1%. Due to the Van Hove singularity in the joint density of states (JDOS), a 2 QL film subjected to an out-of-plane electric field exhibits a considerable absorbance at the absorbance edge. Under the influence of an in-plane external electric field, the dichroism a 6 QL film ranges from -0.3% to 0.3%, while that of a 2 QL film ranges from -1% to 0.5%. The absorbance edge of a 6 QL and a 2 QL film can be shifted about 0.4 and 0.3 eV, respectively, with the application of moderate electric fields about 0.4 Vnm^{-1}. And, with the chemical potential variations about 0.1 and 0.3 eV, the absorbance edge of a 6 QL and a 2 QL film can be shifted about 0.25 and 0.4 eV, respectively.

II. MODEL

We consider a TI thin film, with translational symmetry in the $x - y$ plane, and two surfaces located at $z = \pm L/2$. We assume that the TI thin film is under an external static electric field $\mathbf{E} = (E_x, E_y, E_z)$. We study the optical absorption of the TI thin film. We consider an electromagnetic wave associated with the vector potential $\mathbf{A}(\mathbf{r}, t) = \mathrm{Re}(A_p \hat{\mathbf{e}}_p e^{-i\mathbf{k}_p \cdot \mathbf{r} + i\omega_p t})$. Here, ω_p is the frequency, $\hat{\mathbf{e}}_p$ is the polarization vector, and $\mathbf{k}_p$ is the wave vector of the incident wave. We assume that $\mathbf{k}_p = k_p \hat{\mathbf{e}}_z$, i.e., the wave vector is perpendicular to the thin film. Moreover, $k_p L \ll 1$, i.e., the incident field is almost homogeneous over the thin film. We consider linearly polarized waves with polarization vectors $\hat{\mathbf{e}}_x$ and $\hat{\mathbf{e}}_y$.

III. THE HAMILTONIAN FOR A TI THIN FILM UNDER A STATIC ELECTRIC FIELD

We utilize the Hamiltonian for the bulk TI, including terms to second order in the electron wave vector and to first order in the electric field [34]. Four low-lying states at the Γ point—which are derived from the p orbitals of the Bi and Se atoms—serve as a basis to construct the low-energy effective Hamiltonian $H = H_{\mathrm{TI}} + H_{\mathrm{E}}$ for bulk TI. Indeed,

$$H_{\mathrm{TI}}(\mathbf{k}) = \begin{pmatrix} M_{\mathrm{TI}}(\mathbf{k}) & -iA_1\partial_z & 0 & A_2 k_- \\ -iA_1\partial_z & -M_{\mathrm{TI}}(\mathbf{k}) & A_2 k_- & 0 \\ 0 & A_2 k_+ & M_{\mathrm{TI}}(\mathbf{k}) & iA_1\partial_z \\ A_2 k_+ & 0 & iA_1\partial_z & -M_{\mathrm{TI}}(\mathbf{k}) \end{pmatrix}$$
$$+ \varepsilon_{\mathrm{TI}}(\mathbf{k}) I_{4\times 4}, \qquad (1)$$

where $k_\pm = k_x \pm ik_y$, $k^2 = k_x^2 + k_y^2$, $M_{\mathrm{TI}}(\mathbf{k}) = M + B_1 \partial_z^2 - B_2 k^2$, and $\varepsilon_{\mathrm{TI}}(\mathbf{k}) = C - D_1 \partial_z^2 + D_2 k^2$. The model parameters A_1, A_2, B_1, B_2, C, D_1, D_2, and M can be obtained from

experiments or *ab initio* calculations. The static electric field gives rise to the Hamiltonian

$$H_{\mathrm{E}} = \begin{pmatrix} 0 & iW_z E_z & 0 & iW_\parallel E_- \\ -iW_z E_z & 0 & -iW_\parallel E_- & 0 \\ 0 & iW_\parallel E_+ & 0 & -iW_z E_z \\ -iW_\parallel E_+ & 0 & iW_z E_z & 0 \end{pmatrix}, \qquad (2)$$

where $W_\parallel$ and W_z are real parameters, and $E_\pm = E_x \pm iE_y$.

To obtain an effective Hamiltonian $H^{\mathrm{eff}} = H_{\mathrm{TI}}^{\mathrm{eff}} + H_{\mathrm{E}}^{\mathrm{eff}}$ for a TI thin film under a static electric field, we project H into the surface states and exclude the contribution of the bulk states (see Appendix A). We find that two extra parameters κ_z and $\kappa_\parallel$ are sufficient to express the effective Hamiltonian,

$$H_{\mathrm{E}}^{\mathrm{eff}} = \begin{pmatrix} 0 & -W_\parallel \kappa_\parallel E_- & -W_z \kappa_z E_z & 0 \\ -W_\parallel \kappa_\parallel^* E_+ & 0 & 0 & -W_z \kappa_z^* E_z \\ -W_z \kappa_z^* E_z & 0 & 0 & W_\parallel \kappa_\parallel^* E_- \\ 0 & -W_z \kappa_z E_z & W_\parallel \kappa_\parallel E_+ & 0 \end{pmatrix}. \qquad (3)$$

Now it is apparent that the energies

$$\Xi_x = W_\parallel |\kappa_\parallel| E_x, \quad \Xi_y = W_\parallel |\kappa_\parallel| E_y, \quad \Xi_z = W_z |\kappa_z| E_z \quad (4)$$

are of great importance. Hereafter, we focus on the case $E_x, E_y, E_z > 0$.

We utilize $H_{\mathrm{TI}}^{\mathrm{eff}}$ presented in Ref. [20] to write $H^{\mathrm{eff}} = H_{\mathrm{TI}}^{\mathrm{eff}} + H_{\mathrm{E}}^{\mathrm{eff}}$. For real κ_z and $\kappa_\parallel$ and imaginary $A_L \equiv i\hbar v_{\mathrm{F}}$ (see Appendix A), we find

$$H_{\mathrm{eff}}^{\mathrm{R}}(\mathbf{k}) = \begin{pmatrix} h_+^{\mathrm{R}}(\mathbf{k}) & -\Xi_z \sigma_0 \\ -\Xi_z \sigma_0 & h_-^{\mathrm{R}}(\mathbf{k}) \end{pmatrix}, \qquad (5)$$

where

$$h_{\tau_z}^{\mathrm{R}}(\mathbf{k}) = \varsigma(k) + \hbar v_{\mathrm{F}} (\boldsymbol{\sigma} \times \mathbf{k})_z + \tau_z \sigma_z \vartheta(k) - \tau_z \boldsymbol{\Xi}_\parallel \cdot \boldsymbol{\sigma}, \quad (6)$$

and

$$\varsigma(k) = \varepsilon_L - D_L k^2, \quad \vartheta(k) = \frac{\Delta_L}{2} - B_L k^2.$$

For imaginary κ_z and $\kappa_\parallel$ and real $A_L \equiv \hbar v_{\mathrm{F}}$ (see Appendix A), we find

$$H_{\mathrm{eff}}^{\mathrm{D}}(\mathbf{k}) = \begin{pmatrix} h_+^{\mathrm{D}}(\mathbf{k}) & -i\Xi_z \sigma_z \\ i\Xi_z \sigma_z & h_-^{\mathrm{D}}(\mathbf{k}) \end{pmatrix}, \qquad (7)$$

where

$$h_{\tau_z}^{\mathrm{D}}(\mathbf{k}) = \varsigma(k) + \tau_z \hbar v_{\mathrm{F}} \boldsymbol{\sigma} \cdot \mathbf{k} + \tau_z \sigma_z \vartheta(k) + (\boldsymbol{\Xi} \times \boldsymbol{\sigma})_z. \quad (8)$$

Remarkably, the external electric field not only appears in the off-diagonal blocks, but also in the *diagonal* blocks $h_\pm^{\mathrm{R,D}}(\mathbf{k})$ of the effective Hamiltonian $H_{\mathrm{eff}}^{\mathrm{R,D}}(\mathbf{k})$. The terms $\hbar v_{\mathrm{F}} (\boldsymbol{\sigma} \times \mathbf{k})_z$ and $\tau_z \hbar v_{\mathrm{F}} \boldsymbol{\sigma} \cdot \mathbf{k}$ of the effective Hamiltonians $H_{\mathrm{eff}}^{\mathrm{R}}$ and $H_{\mathrm{eff}}^{\mathrm{D}}$ are reminiscent of Rashba and Dresselhaus spin-orbit interactions, respectively.

A few remarks are in order. (i) For films as thick as or thicker than 6 QL, $\Delta_L = B_L = 0$ [19]. Note that 1 QL is about 1 nm. (ii) The model parameters ε_L, Δ_L, v_{F}, B_L, and D_L can be obtained from *ab initio* calculations or experiments. We adopt $\varepsilon_L = -0.47$ eV, $\Delta_L = 0.252$ eV, $v_{\mathrm{F}} = 4.47 \times 10^5$ ms^{-1}, $B_L = 21.8$ eVÅ^2, and $D_L = -14.4$ eVÅ^2 for a 2 QL film; and $\varepsilon_L = -0.324$ eV, $\Delta_L = 0$, $v_{\mathrm{F}} = 4.28 \times 10^5$ ms^{-1}, $B_L = 0$, and $D_L = -13.0$ eVÅ^2 for a 6 QL film [19,20].

IV. ELECTROABSORPTION OF A TI FILM

The interaction between the photons and the electrons in the TI thin film can be described by the Hamiltonian $H_{\text{eff}}(\mathbf{k} + \frac{e\mathbf{A}}{\hbar}) \equiv H_{\text{eff}}(\mathbf{k}) + H'_{\text{eff}}(\mathbf{k})$, where $-e < 0$ denotes the electron charge. Ignoring the small terms proportional to $\mathbf{A}^2$, we find $H'_{\text{eff}}(\mathbf{k}) = \text{diag}[\text{h}'_+(\mathbf{k}), \text{h}'_-(\mathbf{k})]$, where

$$h'^{R}_{\tau_z}(\mathbf{k}) = -\frac{2e}{\hbar}(D_L + B_L\tau_z\sigma_z)\mathbf{k}\cdot\mathbf{A} + ev_F(\boldsymbol{\sigma}\times\mathbf{A})_z,$$

$$h'^{D}_{\tau_z}(\mathbf{k}) = -\frac{2e}{\hbar}(D_L + B_L\tau_z\sigma_z)\mathbf{k}\cdot\mathbf{A} + \tau_z ev_F\boldsymbol{\sigma}\cdot\mathbf{A}. \quad (9)$$

For a plane wave with $\mathbf{A} = A_p\hat{\mathbf{e}}_p\cos(\omega_p t)$, we write $H'_{\text{eff}}(\mathbf{k}) = \widetilde{H}'_{\text{eff}}(\mathbf{k})e^{-i\omega_p t} + \widetilde{H}'^{\dagger}_{\text{eff}}(\mathbf{k})e^{i\omega_p t}$.

The transition rate for the absorption of a photon is given by the Fermi's golden rule. The total upward transition rate per unit surface area, considering the probability that the initial state Ψ_i is occupied and the final state Ψ_f is empty, is

$$R_{i\to f} = \sum_{i,f}\frac{2\pi}{\hbar S}|\langle\Psi_f|\widetilde{H}'_{\text{eff}}|\Psi_i\rangle|^2\delta(\varepsilon_f - \varepsilon_i - \hbar\omega_p)f(\varepsilon_i)$$
$$\times [1 - f(\varepsilon_f)].$$

The Fermi-Dirac distribution $f(\varepsilon_i) = \frac{1}{1+e^{(\varepsilon_i - \mu)/k_B T}}$, where μ is the chemical potential, k_B is the Boltzmann constant, and T is the temperature. In the limit $T = 0$, $f(\varepsilon_i) = 1 - \Theta(\varepsilon_i - \mu)$, where $\Theta(x)$ denotes the step function. The downward transition rate per unit surface area is

$$R_{f\to i} = \sum_{i,f}\frac{2\pi}{\hbar S}|\langle\Psi_f|\widetilde{H}'_{\text{eff}}|\Psi_i\rangle|^2\delta(\varepsilon_i - \varepsilon_f + \hbar\omega_p)f(\varepsilon_f)$$
$$\times [1 - f(\varepsilon_i)].$$

The net upward transition rate per unit surface area,

$$R(\omega_p, \hat{\mathbf{e}}_p, \boldsymbol{\Xi}) = R_{i\to f}(\omega_p, \hat{\mathbf{e}}_p, \boldsymbol{\Xi}) - R_{f\to i}(\omega_p, \hat{\mathbf{e}}_p, \boldsymbol{\Xi}),$$
$$= \sum_{i,f}\frac{2\pi}{\hbar S}|\langle\Psi_f|\widetilde{H}'_{\text{eff}}|\Psi_i\rangle|^2\delta(\varepsilon_f - \varepsilon_i - \hbar\omega_p)$$
$$\times [f(\varepsilon_i) - f(\varepsilon_f)], \quad (10)$$

can be expressed as a product of an average matrix element and the joint density of states (JDOS),

$$J(\omega_p, \boldsymbol{\Xi}) = \sum_{i,f}J_{i,f}(\omega_p, \boldsymbol{\Xi})$$
$$= \sum_{i,f}\frac{1}{4\pi^2}\int d^2k\,\delta[\varepsilon_f(k) - \varepsilon_i(k) - \hbar\omega_p]. \quad (11)$$

The JDOS informs on the pairs of occupied and unoccupied states, such that the photon of energy $\hbar\omega_p$ can excite an electron between them. Note that the JDOS is, by construction, independent of the chemical potential. When the chemical potential lies in the energy gap, the bands below (above) the chemical potential are fully occupied (unoccupied), and it follows that the average matrix element does not depend on the chemical potential. However, when the chemical potential lies in an energy band, the average matrix element depends on the chemical potential.

The intensity of the incident plane wave is $I_p = \frac{1}{2}c\epsilon_0\omega_p^2 A_p^2$, where ϵ_0 denotes the permittivity of free space. The number

of incident photons per unit area per second is $I_p/(\hbar\omega_p)$. The absorption coefficient, the fraction of photons absorbed by the TI film, is

$$\alpha(\omega_p, \hat{\mathbf{e}}_p, \boldsymbol{\Xi}) = \frac{R(\omega_p, \hat{\mathbf{e}}_p, \boldsymbol{\Xi})}{I_p/(\hbar\omega_p)}. \quad (12)$$

The external electric field breaks the *inversion symmetry* of the system. Whether the incident electromagnetic wave is polarized parallel or perpendicular to the external electric field has a profound effect on the optical transitions between electric field-dependent initial and final states [see Eqs. (9) and (10)]. $\alpha_D(\omega_p, \boldsymbol{\Xi}) = \alpha(\omega_p, \hat{\mathbf{e}}_x, \boldsymbol{\Xi}) - \alpha(\omega_p, \hat{\mathbf{e}}_y, \boldsymbol{\Xi})$ quantifies the dichroism of the system.

For most thicknesses L, A_L is purely imaginary [20]. In the following discussions, we focus on the Rashba-like effective Hamiltonian H^R_{eff}.

A. In-plane static electric field

Here we consider the in-plane static electric field $\mathbf{E} = E_x\hat{\mathbf{e}}_x$. The four eigenvectors of $H^R_{\text{eff}}(\mathbf{k})$,

$$\Psi^{\pm}_{\tau_z=+} = \frac{\begin{pmatrix} \mp\varsigma_1(\mathbf{k}, \Xi_x) - \vartheta(k) \\ i\hbar v_F k_+ + \Xi_x \\ 0 \\ 0 \end{pmatrix}}{\sqrt{2\varsigma_1^2(\mathbf{k}, \Xi_x) \pm 2\varsigma_1(\mathbf{k}, \Xi_x)\vartheta(k)}},$$

$$\Psi^{\pm}_{\tau_z=-} = \frac{\begin{pmatrix} 0 \\ 0 \\ \mp\varsigma_2(\mathbf{k}, \Xi_x) + \vartheta(k) \\ i\hbar v_F k_+ - \Xi_x \end{pmatrix}}{\sqrt{2\varsigma_2^2(\mathbf{k}, \Xi_x) \mp 2\varsigma_2(\mathbf{k}, \Xi_x)\vartheta(k)}}, \quad (13)$$

and corresponding eigenenergies,

$$\varepsilon^{\pm}_{\tau_z=+}(\mathbf{k}, \Xi_x) = \varsigma(k) \pm \varsigma_1(\mathbf{k}, \Xi_x),$$
$$\varepsilon^{\pm}_{\tau_z=-}(\mathbf{k}, \Xi_x) = \varsigma(k) \pm \varsigma_2(\mathbf{k}, \Xi_x), \quad (14)$$

depend on the external electric field. Here,

$$\varsigma_1(\mathbf{k}, \Xi_x) = \sqrt{\vartheta^2(k) + (\hbar v_F k_x)^2 + (\hbar v_F k_y - \Xi_x)^2},$$

$$\varsigma_2(\mathbf{k}, \Xi_x) = \sqrt{\vartheta^2(k) + (\hbar v_F k_x)^2 + (\hbar v_F k_y + \Xi_x)^2}. \quad (15)$$

It is instructive to first consider the case of no electric field. For the optical transition $\Psi^-_{\tau_z=+} \to \Psi^+_{\tau_z=+}$ or $\Psi^-_{\tau_z=-} \to \Psi^+_{\tau_z=-}$, we find

$$J(\omega_p, 0) = \frac{1}{4\pi^2}\int d^2k\,\delta[2\varsigma_1(\mathbf{k}, 0) - \hbar\omega_p$$

$$= \frac{\hbar\omega_p\Theta(\hbar\omega_p - \Delta_L)}{8\pi\sqrt{(\hbar^2 v_F^2 - \Delta_L B_L)^2 + B_L^2(\hbar^2\omega_p^2 - \Delta_L^2)}}. \quad (16)$$

Here the Heaviside step function states that for photon energies below the band gap Δ_L, optical transitions do not occur. JDOS abruptly jumps to $\frac{\Delta_L}{8\pi(\hbar^2 v_F^2 - \Delta_L B_L)}$ at the band edge and, finally, tends to $\frac{1}{8\pi B_L}$ at large photon energies. Among thin films, the 2 QL film whose JDOS exhibits maximum gap, maximum jump at the band edge, and minimum asymptotic

value is of particular interest. Moreover, for both polarization vectors $\hat{\mathbf{e}}_\mathrm{p} = \hat{\mathbf{e}}_x$ and $\hat{\mathbf{e}}_\mathrm{p} = \hat{\mathbf{e}}_y$, the optical transitions $\Psi_{\tau_z=+}^- \to \Psi_{\tau_z=+}^+$ and $\Psi_{\tau_z=-}^- \to \Psi_{\tau_z=-}^+$ lead to

$$\alpha(\omega_\mathrm{p}, \hat{\mathbf{e}}_\mathrm{p}, 0) = \frac{2\pi e^2 v_\mathrm{F}^2 \left[(2B_L k_J^2 + \Delta_L)^2 + \hbar^2 \omega_\mathrm{p}^2 \right]}{2\hbar^2 c \epsilon_0 \omega_\mathrm{p}^3} J(\omega_\mathrm{p}, 0)$$
$$\times \left\{ \Theta[\varsigma(k_J) + \varsigma_1(k_J, 0) - \mu] - \Theta[\varsigma(k_J) - \varsigma_1(k_J, 0) - \mu] \right\}, \quad (17)$$

where

$$k_J^2 = \frac{\Delta_L B_L - \hbar^2 v_\mathrm{F}^2 + \sqrt{(\hbar^2 v_\mathrm{F}^2 - \Delta_L B_L)^2 + B_L^2(\hbar^2 \omega_\mathrm{p}^2 - \Delta_L^2)}}{2B_L^2}.$$

At large photon energies, $\alpha(\omega_\mathrm{p}, \hat{\mathbf{e}}_\mathrm{p}, 0) \approx \frac{e^2 v_\mathrm{F}^2}{4c\epsilon_0 B_L} \frac{1}{\omega_\mathrm{p}}$. Apparently, the TI thin film exhibits no dichroism in the absence of the external static electric field.

For films as thick as or thicker than 6 QL, the surface-state gap is *closed* when the electric field is zero. Here, $\varsigma_1(\mathbf{k}, 0) = \hbar v_\mathrm{F} k$ is linear in k. For the optical transition $\Psi_{\tau_z=+}^- \to \Psi_{\tau_z=+}^+$ or $\Psi_{\tau_z=-}^- \to \Psi_{\tau_z=-}^+$, we find

$$J_\mathrm{6QL}(\omega_\mathrm{p}, 0) = \frac{\omega_\mathrm{p}}{8\pi \hbar v_\mathrm{F}^2}. \quad (18)$$

In the absence of the static electric field, the absorbance is $\frac{\pi}{2}\alpha_\mathrm{fine}$ in a chemical potential-dependent frequency window,

$$\alpha_\mathrm{6QL}(\omega_\mathrm{p}, \hat{\mathbf{e}}_\mathrm{p}, 0) = \frac{\pi}{2}\alpha_\mathrm{fine} \left\{ \Theta[\varsigma(k_J) + \hbar v_\mathrm{F} k_J - \mu] - \Theta[\varsigma(k_J) - \hbar v_\mathrm{F} k_J - \mu] \right\}, \quad (19)$$

where $k_J = \frac{\omega_\mathrm{p}}{2v_\mathrm{F}}$. Notably, the absorbance $\frac{\pi}{2}\alpha_\mathrm{fine} \approx 1.1\%$ is half the absorbance of graphene.

The static electric field alters the optical response of TI thin film. This can be traced back to electric field-dependent dispersion curves $\varepsilon_\pm^\pm(\mathbf{k}, \Xi_x) - \varsigma(k)$. Figures 1(a1) and 1(b1) show that as Ξ_x increases, the doubly degenerate gapless Dirac cone of a 6 QL film evolves into nondegenerate gapless Dirac hyperbolas split along the k_y axis. In other words, the Dirac points merely shift from $(k_x = 0, k_y = 0)$ to $(k_x = 0, k_y = \pm\Xi_x/\hbar v_\mathrm{F})$. It follows that the JDOS of allowed transitions does not depend on the static electric field,

$$J_\mathrm{6QL}(\omega_\mathrm{p}, \Xi_x) = \frac{\omega_\mathrm{p}}{8\pi \hbar v_\mathrm{F}^2}, \quad (20)$$

shown in Fig. 1(c1). For films thinner than 6 QL, the story is rather different. Figures 1(a2) and 1(b2) show that as Ξ_x increases, the doubly degenerate gapped hyperbola of a TI film evolves into nondegenerate gapped hyperbolas split along the k_y axis. Nevertheless, the gap Δ_gap strongly depends on the in-plane static electric field. We find (see Appendix B)

$$\Delta_\mathrm{gap} = 2\sqrt{\left(B_L k_\mathrm{gap}^2 - \frac{\Delta_L}{2}\right)^2 + (\hbar v_\mathrm{F} k_\mathrm{gap} - \Xi_x)^2}, \quad (21)$$
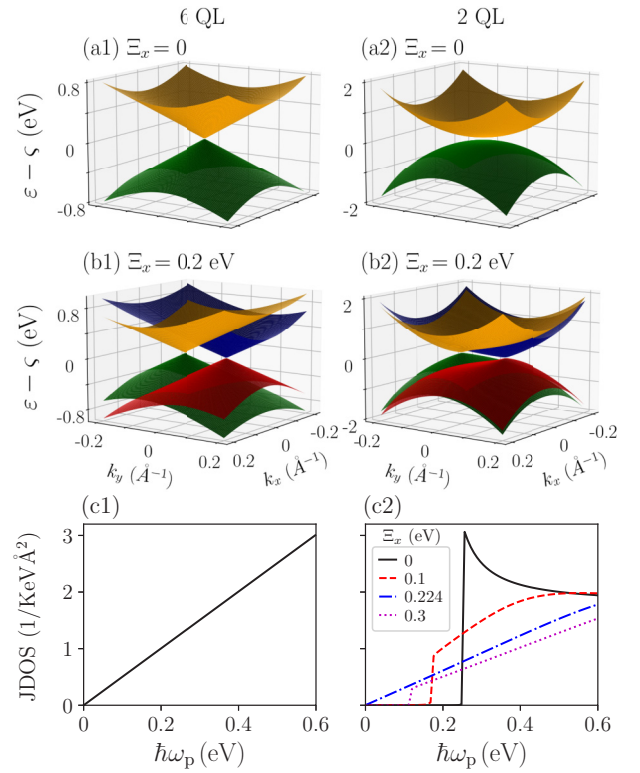
FIG. 1. $\varepsilon_+^+ - \varsigma$ (blue), $\varepsilon_+^- - \varsigma$ (red), $\varepsilon_-^+ - \varsigma$ (orange), and $\varepsilon_-^- - \varsigma$ (green) of a 6 QL film, as a function of k_x and k_y when (a1) $\Xi_x = 0$ and (b1) $\Xi_x = 0.2$ eV. (c1) J as a function of ω_p for various Ξ_x. Similar plots for a 2 QL film are in (a2)–(c2).

where

$$k_\mathrm{gap} = \left[\frac{\hbar v_\mathrm{F} \Xi_x}{4B_L^2} + \sqrt{\frac{\hbar^2 v_\mathrm{F}^2 \Xi_x^2}{16B_L^4} + \frac{(\hbar^2 v_\mathrm{F}^2 - \Delta_L B_L)^3}{216B_L^6}} \right]^{\frac{1}{3}}$$
$$+ \left[\frac{\hbar v_\mathrm{F} \Xi_x}{4B_L^2} - \sqrt{\frac{\hbar^2 v_\mathrm{F}^2 \Xi_x^2}{16B_L^4} + \frac{(\hbar^2 v_\mathrm{F}^2 - \Delta_L B_L)^3}{216B_L^6}} \right]^{\frac{1}{3}}. \quad (22)$$

It follows that two bands $\varepsilon_{\tau_z=+}^\pm$ touch each other when $\Xi_x = \Xi_x^\times = \hbar v_\mathrm{F}\sqrt{\frac{\Delta_L}{2B_L}}$. The closing and reopening of the energy gap at $\Xi_x = \Xi_x^\times$ signifies a topological phase transition. Remarkably, $\Xi_x^\times$ depends on the film thickness L. For a 2 QL film, $\Xi_x^\times = 0.224$ eV. In addition,

$$\Delta_\mathrm{gap} \approx \sqrt{\Delta_L^2 - \frac{4\Delta_L B_L}{\hbar^2 v_\mathrm{F}^2 - \Delta_L B_L} \Xi_x^2} \quad (23)$$

in the limit $\Xi_x \to 0$. As Ξ_x increases, Δ_gap first decreases from Δ_L, becomes zero at $\Xi_x^\times$, and then increases. Generally, $2\varsigma_1(\mathbf{k}, \Xi_x) \approx \Delta_\mathrm{gap} + \wp_x k_x^2 + \wp_y(k_y - k_\mathrm{gap})^2$ in the vicinity of the point $(k_x = 0, k_y = k_\mathrm{gap})$, where

$$\wp_x = \frac{4B_L^2 k_\mathrm{gap}^2 - 2B_L \Delta_L + 2\hbar^2 v_\mathrm{F}^2}{\Delta_\mathrm{gap}} > 0,$$
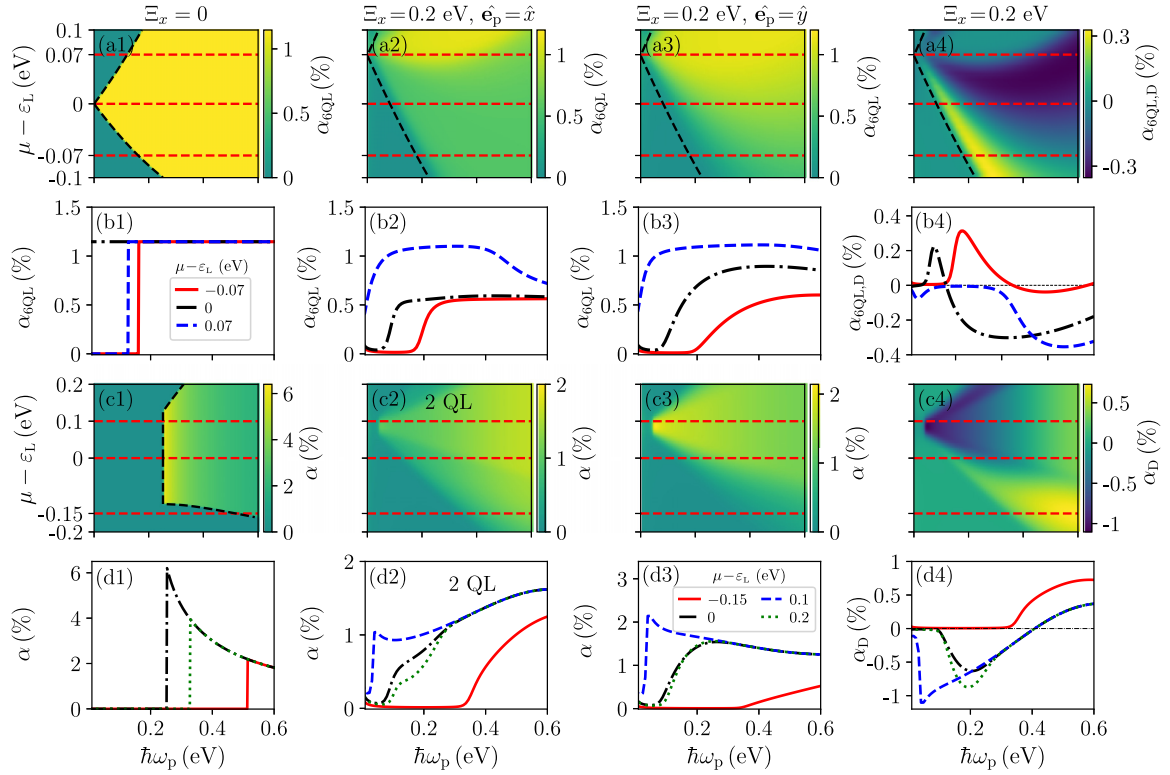$$\wp_y = \frac{12B_L^2 k_\mathrm{gap}^2 - 2B_L \Delta_L + 2\hbar^2 v_\mathrm{F}^2}{\Delta_\mathrm{gap}} > 0. \quad (24)$$

FIG. 2. Contour plot of (a1) α_{6QL} when $\Xi_x = 0$, (a2) α_{6QL} when $\Xi_x = 0.2$ eV and $\hat{\mathbf{e}}_p = \hat{\mathbf{e}}_x$, (a3) α_{6QL} when $\Xi_x = 0.2$ eV and $\hat{\mathbf{e}}_p = \hat{\mathbf{e}}_y$, and (a4) $\alpha_{6QL,D}$ when $\Xi_x = 0.2$ eV, for a 6 QL film. Lines cut for $\mu - \varepsilon_L = -0.07$, 0, and 0.07 eV are in (b1)–(b4). Similar plots for a 2 QL film are in (c1)–(c4) and (d1)–(d4).

It follows that

$$J(\omega_p, \Xi_x) \approx \frac{1}{4\pi \sqrt{\wp_x \wp_y}} \Theta(\hbar\omega_p - \Delta_{\text{gap}}) \qquad (25)$$

exhibits an abrupt jump when $\Xi_x \neq \Xi_x^\times$ and $\hbar\omega_p \to \Delta_{\text{gap}}$. Figure 1(c2) emphasizes that the static electric field can be invoked to tailor the JDOS of a 2 QL film: For example, one can engineer a gapped and decreasing JDOS at $\Xi_x = 0$, a gapless and increasing JDOS at $\Xi_x = \Xi_x^\times = 0.224$ eV, and a gapped and almost linearly increasing JDOS at $\Xi_x = 0.3$ eV.

The dependence of absorbance on the frequency ω_p and polarization vector $\hat{\mathbf{e}}_p$ of the incident wave, and the chemical potential μ, is illustrated in Fig. 2. The contour plots in Figs. 2(a1)–2(a4) show that when Ξ_x is zero, a 6 QL film exhibits a constant absorption coefficient $\frac{\pi}{2}\alpha_{\text{fine}} \approx 1.1\%$ in a considerable domain. As one increases Ξ_x to 0.2 eV, this domain shrinks differently for different polarization vectors, and the dichroism emerges. Indeed, in a noticeable domain, $\alpha_{6QL,D}$ is as large as $\pm0.3\%$. At a glance, it is clear that the absorption edge strongly depends on the chemical potential. For typical $\mu - \varepsilon_L = -0.07$, 0, and 0.07 eV, previous data are better shown in Figs. 2(b1)–2(b4). Similar plots for a 2 QL film are in Figs. 2(c1)–2(c4) and Figs. 2(d1)–2(d4). When Ξ_x is zero, absorbance edges greater than 0.252 eV and absorbances as large as 6% are easily noticeable. The absorbance behaves much like the JDOS: The absorbance vanishes below the edge, abruptly rises to its maximum, and then monotonically decreases. As one increases Ξ_x to 0.2 eV, absorbance edges as small as 0.018 eV and absorbances below 2%, yet above $\frac{\pi}{2}\alpha_{\text{fine}} \approx 1.1\%$, are principal features. Now

the absorbance smoothly rises from zero at the absorbance edge, rises to its maximum, and then decreases. The dichroism is also quite considerable: α_D ranges from -1% to 0.5%. The *tunability* of the absorbance and dichroism spectra—in particular their edges and maxima—via the static electric field and the chemical potential is vividly clear.

B. Out-of-plane static electric field

Here we consider the out-of-plane static electric field $\mathbf{E} = E_z \hat{\mathbf{e}}_z$. The four eigenvectors of $H_{\text{eff}}^R(\mathbf{k})$,

$$\Psi_I^\pm = \frac{\begin{pmatrix} ie^{-i\theta_k}(\hbar v_F k - \Xi_z) \\ \pm\zeta_1(k, \Xi_z) - \vartheta(k) \\ ie^{-i\theta_k}[\pm\zeta_1(k, \Xi_z) - \vartheta(k)] \\ \hbar v_F k - \Xi_z \end{pmatrix}}{2\sqrt{\zeta_1^2(k, \Xi_z) \mp \zeta_1(k, \Xi_z)\vartheta(k)}},$$

$$\Psi_{II}^\pm = \frac{\begin{pmatrix} ie^{-i\theta_k}(\hbar v_F k - \Xi_z) \\ \pm\zeta_2(k, \Xi_z) - \vartheta(k) \\ ie^{-i\theta_k}[\pm\zeta_2(k, \Xi_z) - \vartheta(k)] \\ \hbar v_F k - \Xi_z \end{pmatrix}}{2\sqrt{\zeta_2^2(k, \Xi_z) \mp \zeta_2(k, \Xi_z)\vartheta(k)}}, \qquad (26)$$

and corresponding eigenenergies,

$$\varepsilon_I^\pm(k, \Xi_z) = \varsigma(k) \pm \zeta_1(k, \Xi_z),$$
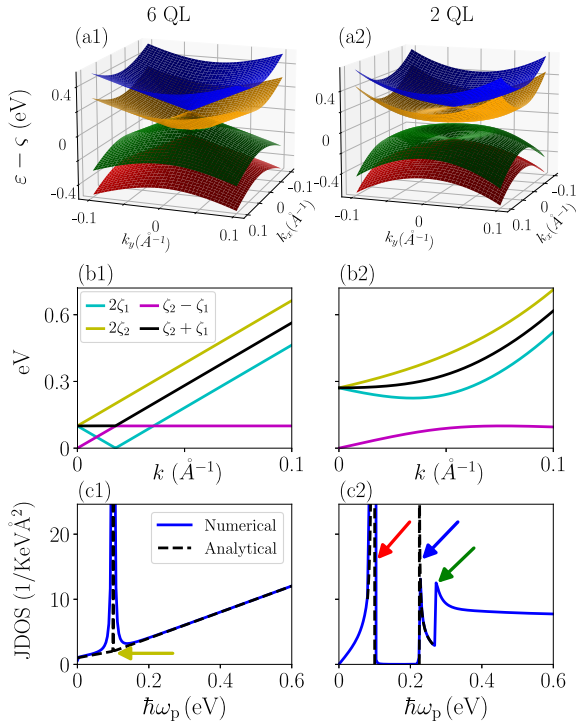$$\varepsilon_{II}^\pm(k, \Xi_z) = \varsigma(k) \pm \zeta_2(k, \Xi_z), \qquad (27)$$

FIG. 3. (a1) $\varepsilon_{\mathrm{I}}^+ - \varsigma$ (orange), $\varepsilon_{\mathrm{I}}^- - \varsigma$ (green), $\varepsilon_{\mathrm{II}}^+ - \varsigma$ (blue), and $\varepsilon_{\mathrm{II}}^- - \varsigma$ (red) as a function of k_x and k_y, (b1) $2\zeta_1$, $2\zeta_2$, and $\zeta_2 \pm \zeta_1$ as a function of k, and (c1) J as a function of ω_p for a 6 QL film. Similar plots for a 2 QL film are in (a2)–(c2). In all plots, $\Xi_z = 0.05$ eV.

depend on the external electric field. Here, $\theta_k = \arctan(k_y/k_x)$ and

$$\zeta_1(k, \Xi_z) = \sqrt{\vartheta^2(k) + (\hbar v_\mathrm{F} k - \Xi_z)^2},$$
$$\zeta_2(k, \Xi_z) = \sqrt{\vartheta^2(k) + (\hbar v_\mathrm{F} k + \Xi_z)^2}. \quad (28)$$

For films as thick as or thicker than 6 QL, $\Delta_L = B_L = 0$. It follows that $\varepsilon_{\mathrm{I,6QL}}^\pm(k, \Xi_z) = \varsigma(k) \pm |\hbar v_\mathrm{F} k - \Xi_z|$ and $\varepsilon_{\mathrm{II,6QL}}^\pm(k, \Xi_z) = \varsigma(k) \pm (\hbar v_\mathrm{F} k + \Xi_z)$. Evidently, the influence of the electric field on the optical response of TI thin film is rooted in the electric field-dependent dispersion curves. Exemplary dispersion curves for a 6 QL film when $\Xi_z = 0$ and 0.05 eV are shown in Figs. 1(a1) and 3(a1), respectively. The pertinent energy difference between the bands and the total JDOS for $\Xi_z = 0.05$ eV is shown in Figs. 3(b1) and 3(c1). Taking into account all *six* transitions between four bands $\varepsilon_{\mathrm{I,II,6QL}}^\pm$, we find

$$J_\mathrm{6QL}(\omega_\mathrm{p}, \Xi_z) = \frac{\hbar\omega_\mathrm{p} + 2\Xi_z + (\hbar\omega_\mathrm{p} - 2\Xi_z)\Theta(\hbar\omega_\mathrm{p} - 2\Xi_z)}{4\pi\hbar^2 v_\mathrm{F}^2}$$
$$+ \frac{k_\mathrm{c}^2}{4\pi}\delta(\hbar\omega_\mathrm{p} - 2\Xi_z), \quad (29)$$

where k_c denotes the cutoff wavelength. Note that the slope of the J_6QL abruptly changes at frequency $2\Xi_z/\hbar$ [see the yellow arrow in Fig. 3(c1)].

Now we focus on thin films. Exemplary dispersion curves for a 2 QL film when $\Xi_z = 0$ and 0.05 eV are shown in Figs. 1(a2) and 3(a2), respectively. The pertinent energy difference between the bands, i.e., $2\zeta_1$, $2\zeta_2$, and $\zeta_2 \pm \zeta_1$, and the
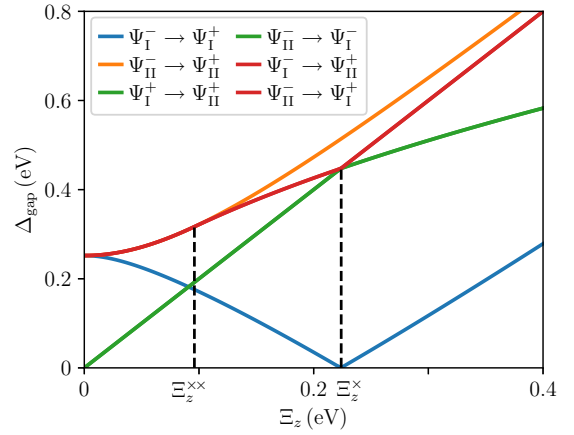

FIG. 4. Δ_gap pertaining to various optical transitions in a 2 QL film, as a function of Ξ_z.

total JDOS for $\Xi_z = 0.05$ eV is depicted in Figs. 3(b2) and 3(c2). The salient features of JDOS can be inferred from the behavior of dispersion curves near the point $k = 0$ and the critical point k_cr. We find the following:

(i) In the vicinity of the critical point,

$$k_\mathrm{cr} = \left[\frac{\hbar v_\mathrm{F} \Xi_z}{4B_L^2} + \sqrt{\frac{\hbar^2 v_\mathrm{F}^2 \Xi_z^2}{16B_L^4} + \frac{\left(\hbar^2 v_\mathrm{F}^2 - \Delta_L B_L\right)^3}{216B_L^6}}\right]^{\frac{1}{3}}$$
$$+ \left[\frac{\hbar v_\mathrm{F} \Xi_z}{4B_L^2} - \sqrt{\frac{\hbar^2 v_\mathrm{F}^2 \Xi_z^2}{16B_L^4} + \frac{\left(\hbar^2 v_\mathrm{F}^2 - \Delta_L B_L\right)^3}{216B_L^6}}\right]^{\frac{1}{3}}, \quad (30)$$

indeed, $2\zeta_1(k, \Xi_z) \approx \Delta_\mathrm{gap} + \wp_2(k - k_\mathrm{cr})^2$, where

$$\Delta_\mathrm{gap} = 2\sqrt{\left(B_L k_\mathrm{cr}^2 - \frac{\Delta_L}{2}\right)^2 + (\hbar v_\mathrm{F} k_\mathrm{cr} - \Xi_z)^2},$$
$$\wp_2 = \frac{12 B_L^2 k_\mathrm{cr}^2 - 2B_L \Delta_L + 2\hbar^2 v_\mathrm{F}^2}{\Delta_\mathrm{gap}}. \quad (31)$$

As Ξ_z increases, Δ_gap first decreases, becomes zero at $\Xi_z^\times = \hbar v_\mathrm{F}\sqrt{\frac{\Delta_L}{2B_L}}$, and then increases (see the blue curve in Fig. 4). For the optical transition $\Psi_\mathrm{I}^- \to \Psi_\mathrm{I}^+$,

$$J(\omega_\mathrm{p}, \Xi_z)$$
$$\approx \frac{1}{4\pi\sqrt{\wp_2}}\frac{\Theta(\hbar\omega_\mathrm{p} - \Delta_\mathrm{gap})}{\sqrt{\hbar\omega_\mathrm{p} - \Delta_\mathrm{gap}}}\left[k_\mathrm{cr} + \sqrt{\frac{\hbar\omega_\mathrm{p} - \Delta_\mathrm{gap}}{\wp_2}}\right.$$
$$\left. + \left(k_\mathrm{cr} - \sqrt{\frac{\hbar\omega_\mathrm{p} - \Delta_\mathrm{gap}}{\wp_2}}\right)\Theta\left(k_\mathrm{cr} - \sqrt{\frac{\hbar\omega_\mathrm{p} - \Delta_\mathrm{gap}}{\wp_2}}\right)\right]$$
$$\quad (32)$$

exhibits a inverse-square-root singular behavior when $\hbar\omega_\mathrm{p} \to \Delta_\mathrm{gap}$ and no abrupt jump when $\hbar\omega_\mathrm{p} \to \Delta_\mathrm{gap} + \wp_2 k_\mathrm{cr}^2$ [see the blue arrow in Fig. 3(c2)].

(ii) In the vicinity of $k = 0$, indeed, $2\zeta_2(k, \Xi_z) \approx \Delta_{\text{gap}} + \wp_1 k$, where

$$\Delta_{\text{gap}} = 2\sqrt{\frac{\Delta_L^2}{4} + \Xi_z^2}, \quad \wp_1 = \frac{2\hbar v_{\text{F}} \Xi_z}{\sqrt{\frac{\Delta_L^2}{4} + \Xi_z^2}}. \quad (33)$$

Here, Δ_{gap} monotonically increases from Δ_L as Ξ_z increases (see the orange curve in Fig. 4). For the optical transition $\Psi_{\text{II}}^- \to \Psi_{\text{II}}^+$,

$$J(\omega_{\text{p}}, \Xi_z) \approx \frac{(\hbar\omega_{\text{p}} - \Delta_{\text{gap}})}{2\pi\wp_1^2} \Theta(\hbar\omega_{\text{p}} - \Delta_{\text{gap}}) \quad (34)$$

exhibits no abrupt jump when $\hbar\omega_{\text{p}} \to \Delta_{\text{gap}}$.

(iii) In the vicinity of the critical point,

$$k_{\text{cr}} = \begin{cases} \sqrt{\frac{\Delta_L}{2B_L}}, & \Xi_z < \Xi_z^{\times}, \\ \sqrt{\frac{\sqrt{16B_L^2 \Xi_z^2 + \left(\hbar^2 v_{\text{F}}^2 - 2B_L\Delta_L\right)^2} - \hbar^2 v_{\text{F}}^2}{4B_L^2}}, & \Xi_z > \Xi_z^{\times}, \end{cases} \quad (35)$$

indeed, $\zeta_2 - \zeta_1 \approx \Delta_{\text{gap}} + \wp_2(k - k_{\text{cr}})^2$, where

$$\Delta_{\text{gap}} = \sqrt{\left(B_L k_{\text{cr}}^2 - \frac{\Delta_L}{2}\right)^2 + (\hbar v_{\text{F}} k_{\text{cr}} + \Xi_z)^2}$$
$$- \sqrt{\left(B_L k_{\text{cr}}^2 - \frac{\Delta_L}{2}\right)^2 + (\hbar v_{\text{F}} k_{\text{cr}} - \Xi_z)^2}, \quad (36)$$

and $\wp_2 < 0$. Notably, Δ_{gap} monotonically increases from zero as Ξ_z increases, although with a smaller rate when $\Xi_z > \Xi_z^{\times}$ (see the green curve in Fig. 4). For the optical transitions $\Psi_{\text{I}}^+ \to \Psi_{\text{II}}^+$ and $\Psi_{\text{II}}^- \to \Psi_{\text{I}}^-$,

$$J(\omega_{\text{p}}, \Xi_z) \approx \frac{1}{4\pi\sqrt{|\wp_2|}} \frac{\Theta(\Delta_{\text{gap}} - \hbar\omega_{\text{p}})}{\sqrt{\Delta_{\text{gap}} - \hbar\omega_{\text{p}}}} \left[k_{\text{cr}} + \sqrt{\frac{\Delta_{\text{gap}} - \hbar\omega_{\text{p}}}{|\wp_2|}} \right.$$
$$+ \left(k_{\text{cr}} - \sqrt{\frac{\Delta_{\text{gap}} - \hbar\omega_{\text{p}}}{|\wp_2|}} \right)$$
$$\left. \Theta\left(k_{\text{cr}} - \sqrt{\frac{\Delta_{\text{gap}} - \hbar\omega_{\text{p}}}{|\wp_2|}} \right) \right] \quad (37)$$

exhibits a inverse-square-root singular behavior when $\hbar\omega_{\text{p}} \to \Delta_{\text{gap}}$ and no abrupt jump when $\hbar\omega_{\text{p}} \to \Delta_{\text{gap}} - |\wp_2| k_{\text{cr}}^2$ [see the red arrow in Fig. 3(c2)].

(iv) $\Xi_z^{\times\times} = \Xi_z^{\times} \sqrt{\frac{1}{2} - \frac{B_L\Delta_L}{2\hbar^2 v_{\text{F}}^2}}$ depends on the film thickness L. For a 2 QL film, $\Xi_z^{\times\times} \approx 0.1$ eV. If $\Xi_z < \Xi_z^{\times\times}$, then $\zeta_2 + \zeta_1 \approx \Delta_{\text{gap}} + \wp_2 k^2$ in the vicinity of $k = 0$. Here,

$$\Delta_{\text{gap}} = 2\sqrt{\frac{\Delta_L^2}{4} + \Xi_z^2}, \quad \wp_2 = \frac{\hbar^2 v_{\text{F}}^2 - \Delta_L B_L}{\left(\frac{\Delta_L^2}{4} + \Xi_z^2\right)^{\frac{1}{2}}} - \frac{\hbar^2 v_{\text{F}}^2 \Xi_z^2}{\left(\frac{\Delta_L^2}{4} + \Xi_z^2\right)^{\frac{3}{2}}}. \quad (38)$$

Indeed, Δ_{gap} monotonically increases from Δ_L as Ξ_z increases towards $\Xi_z^{\times\times}$ (see the red curve in Fig. 4). For the optical transitions $\Psi_{\text{I}}^- \to \Psi_{\text{II}}^+$ and $\Psi_{\text{II}}^- \to \Psi_{\text{I}}^+$,

$$J(\omega_{\text{p}}, \Xi_z) \approx \frac{1}{4\pi\wp_2} \Theta(\hbar\omega_{\text{p}} - \Delta_{\text{gap}}) \quad (39)$$
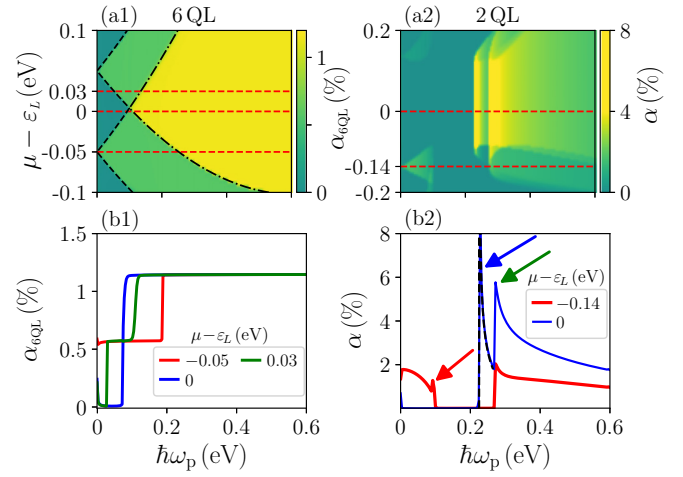

FIG. 5. (a1) Contour plot of α_{6QL}. (b1) α_{6QL} vs ω_{p} for various $\mu - \varepsilon_L$. Similar plots for a 2 QL film are in (a2) and (b2). In all plots, $\Xi_z = 0.05$ eV.

exhibits an abrupt jump when $\hbar\omega_{\text{p}} \to \Delta_{\text{gap}}$ [see the green arrow in Fig. 3(c2)]. If $\Xi_z^{\times\times} < \Xi_z$, then $\zeta_2 + \zeta_1 \approx \Delta_{\text{gap}} + \wp_2(k - k_{\text{cr}})^2$ in the vicinity of the critical point,

$$k_{\text{cr}} = \begin{cases} \sqrt{\frac{\sqrt{16B_L^2 \Xi_z^2 + \left(\hbar^2 v_{\text{F}}^2 - 2B_L\Delta_L\right)^2} - \hbar^2 v_{\text{F}}^2}{4B_L^2}}, & \Xi_z^{\times\times} < \Xi_z < \Xi_z^{\times}, \\ \sqrt{\frac{\Delta_L}{2B_L}}, & \Xi_z > \Xi_z^{\times}. \end{cases} \quad (40)$$

Here,

$$\Delta_{\text{gap}} = \sqrt{\left(B_L k_{\text{cr}}^2 - \frac{\Delta_L}{2}\right)^2 + (\hbar v_{\text{F}} k_{\text{cr}} + \Xi_z)^2}$$
$$+ \sqrt{\left(B_L k_{\text{cr}}^2 - \frac{\Delta_L}{2}\right)^2 + (\hbar v_{\text{F}} k_{\text{cr}} - \Xi_z)^2}, \quad (41)$$

and $\wp_2 > 0$. Notably, Δ_{gap} monotonically increases as Ξ_z increases from $\Xi_z^{\times\times}$, although with a larger rate when $\Xi_z > \Xi_z^{\times}$ (see the red curve in Fig. 4). Equation (32) implies that $J(\omega_{\text{p}}, \Xi_z)$ exhibits a inverse-square-root singular behavior when $\hbar\omega_{\text{p}} \to \Delta_{\text{gap}}$ and no abrupt jump when $\hbar\omega_{\text{p}} \to \Delta_{\text{gap}} + \wp_2 k_{\text{cr}}^2$.

The absorbance inherits the main features of JDOS, thus we now pay attention to the *tunability* of the absorbance spectrum via the static electric field and the chemical potential. Considering *four* allowed optical transitions $\Psi_{\text{I}}^- \to \Psi_{\text{II}}^-$, $\Psi_{\text{I}}^- \to \Psi_{\text{II}}^+$, $\Psi_{\text{I}}^+ \to \Psi_{\text{II}}^-$, and $\Psi_{\text{I}}^+ \to \Psi_{\text{II}}^+$, the absorbance of a film as thick as or thicker than 6 QL reads

$$\alpha_{\text{6QL}}(\omega_{\text{p}}, \hat{\mathbf{e}}_{\text{p}}, \Xi_z) = \frac{\pi}{4}\alpha_{\text{fine}}\{\Theta[\varsigma(k_J) + \Xi_z + \hbar v_{\text{F}} k_J - \mu]$$
$$+ \Theta[\varsigma(k_J) - \Xi_z + \hbar v_{\text{F}} k_J - \mu]$$
$$- \Theta[\varsigma(k_J) + \Xi_z - \hbar v_{\text{F}} k_J - \mu]$$
$$- \Theta[\varsigma(k_J) - \Xi_z - \hbar v_{\text{F}} k_J - \mu]\}, \quad (42)$$

where $k_J = \frac{\omega_{\text{p}}}{2v_{\text{F}}}$ and the polarization vector is either $\hat{\mathbf{e}}_x$ or $\hat{\mathbf{e}}_y$. Figures 2(a1) and 5(a1) show absorbance of a 6 QL film as

a function of ω_p and μ, for the cases of $\Xi_z = 0$ and 0.05 eV, respectively. When Ξ_z is zero, a 6 QL film exhibits a constant absorption coefficient $\frac{\pi}{2}\alpha_{\text{fine}} \approx 1.1\%$ in a considerable domain. As one increases Ξ_z to 0.05 eV, new domains of constant absorption coefficient $\frac{\pi}{4}\alpha_{\text{fine}} \approx 0.55\%$ and $\frac{\pi}{2}\alpha_{\text{fine}} \approx 1.1\%$ appear. This is further illustrated in Figs. 2(b1) and 5(b1) that both the external electric field and the chemical potential have a strong impact on the absorbance. Figures 2(c1) and 5(a2) show absorbance of a 2 QL film as a function of ω_p and μ, for the cases of $\Xi_z = 0$ and 0.05 eV, respectively. When Ξ_z is zero, absorbances as large as 6% are achievable. As one increases Ξ_z to 0.05 eV, quite large absorbances at the absorbance edges are realizable. For typical $\mu - \varepsilon_L = 0$ and -0.15 eV, previous data are better shown in Figs 2(d1) and 5(b2).

V. DISCUSSION AND CONCLUSION

A few remarks are in order.

(i) We have assumed that the impurity and phonon scattering mechanisms are ignorable in a clean sample held at low temperature. Thus we have not taken into account intraband transitions which lead to a Drude-like term in the absorbance of TI thin film. The intraband transitions are notable when the photon energy $\hbar\omega_p$ is below 0.1 eV.

(ii) Due to the quantum confinement effect, the bulk and thin films of TI have distinct band structures. In other words, the bulk states and the so-called quantum-well states have different energies. Indeed, the energy separation between the quantum-well states increases as the film thickness L decreases. For Bi_2Se_3, the bulk and quantum-well states exhibit band gaps about 0.3 eV and 0.7–0.9 eV, respectively (see Fig. 3 in Ref. [20] and Fig. 1(c) in Ref. [29]). It follows that transitions between the quantum-well states contribute to the absorbance of TI thin films when the photon energy $\hbar\omega_p$ is above 0.7 eV [29]. On the other hand, the overlap between the surface state and quantum-well state wave functions is quite small, thus the optical transition between these states is quite weak.

(iii) The control of the chemical potential in TIs, even in Bi_2Se_3, is no longer elusive [13,35,36]. It is reported that 10-nm-thick Bi_2Se_3 films grown on $SrTiO_3$ allow for tunability in carrier density with a back gate [35]. It is also demonstrated that by using the combination of SiO_2/Si bottom gating and the doping of 2,3,5,6-tetrafluoro-7,7,8,8-tetracyanoquinodimethane (F4TCNQ) molecules on the top surface, the chemical potential can be well controlled [36].

(iv) We have assumed that the quantum-well state conduction band is not populated. This naturally translates into a bound on the chemical potential. The energy difference between the surface state and the quantum-well state conduction bands is about 0.1 and 0.2 eV in 6 QL and 2 QL Bi_2Se_3 films, respectively (see Fig. 2 in Ref. [19] for films grown on a double-layer-graphene-terminated 6H-SiC substrate; see, also, Fig. 1 in Ref. [37] for films grown on InP and Fig. 3 in Ref. [38] for films grown on AlN). Encouraged by the ongoing advances in the control of the chemical potential in Bi_2Se_3, we have studied the whole interval $|\mu - \varepsilon_L| < 0.1$–0.2 eV.

(v) A close look at Figs. 2 and 5 reveals that even in the absence of the electric field [see, also, Eq. (19)],

$$\alpha_{\text{6QL}}(\mu) \neq \alpha_{\text{6QL}}(-\mu), \alpha(\mu) \neq \alpha(-\mu). \tag{43}$$

This is rooted in the *electron-hole asymmetry*: First, $\varepsilon_{\pm}^{+}(\mathbf{k}, 0) \neq -\varepsilon_{\pm}^{-}(\mathbf{k}, 0)$ unless $\varsigma(k) = \varepsilon_L - D_L k^2$ is absent. Second, according to the Fermi-Dirac distribution, whether an electronic state of the high [low] band is empty [occupied] depends on $\varepsilon_{\pm}^{+}(\mathbf{k}, 0) - \mu$ [$\varepsilon_{\pm}^{-}(\mathbf{k}, 0) - \mu$] rather than mere $\varepsilon_{\pm}^{+}(\mathbf{k}, 0)$ [$\varepsilon_{\pm}^{-}(\mathbf{k}, 0)$]. Note that the electron-hole asymmetry does not manifest in the JDOS, which portrays the splitting of high and low bands. Using magneto-infrared spectroscopy, the intrinsic electron-hole asymmetry of surface states in TI thin films was recently demonstrated [31].

(vi) As expected, the features of the JDOS are reflected in the absorbance. This can be confirmed by a comparison of Figs. 3(c2) and 5(b2) (particularly note the red, blue, and green arrows).

(vii) The Van Hove singularity in the JDOS differentiates between a 6 QL and a 2 QL film [see Eqs. (32) and (37)]: The maximum absorbance of a 6 QL film is 1.1%, while that of a 2 QL film subjected to an out-of-plane external electric field is considerable at the absorbance edge.

(viii) We have considered high-quality Bi_2Se_3 thin films which are available via molecular beam epitaxy and chemical vapor deposition. We have not considered the influence of disorder on the absorbance of TI thin films. However, we intuitively expect the salient features of absorbance due to the Van Hove singularity to persist despite the presence of weak nonmagnetic impurities.

(ix) We have studied the absorbance of TI thin films in view of electro-optic modulators and switches. Thus there is a good reason to pay attention to the absorbance edge. Indeed, the absorbance edge strongly depends on *both* the static electric field and the chemical potential. For films as thick as or thicker than 6 QL, an analysis merely based on the conservation of energy in the optical transition from an occupied state to an empty state shows that

$$\omega_{\text{edge}} = \begin{cases} \frac{\frac{2D_L\Xi_x}{\hbar v_F} - \hbar v_F + \sqrt{\hbar^2 v_F^2 - 4D_L(\mu - \varepsilon_L + \Xi_x)}}{-D_L/v_F}, & \mu - \varepsilon_L > \frac{-D_L\Xi_x^2}{\hbar^2 v_F^2}, \\ \frac{-\frac{2D_L\Xi_x}{\hbar v_F} + \hbar v_F - \sqrt{\hbar^2 v_F^2 - 4D_L(\mu - \varepsilon_L + \Xi_x)}}{-D_L/v_F}, & \mu - \varepsilon_L < \frac{-D_L\Xi_x^2}{\hbar^2 v_F^2}, \end{cases} \tag{44}$$

when $\Xi_x \neq 0$. Note that $-D_L > 0$. ω_{edge} is not a function of only $\mu - \varepsilon_L + \Xi_x$, but a function of both $\mu - \varepsilon_L$ and Ξ_x. It follows that $\mu - \varepsilon_L$ and Ξ_x differently influence ω_{edge}. The above analytical estimate is shown as a black dotted line in the contour plots in Figs. 2(a1)–2(a4). Naively neglecting the electron-hole asymmetry, one finds that $\omega_{\text{edge}} = \frac{2|\mu|}{\hbar}$, which implies that the absorbance edge does not depend on the in-plane static electric field.

(x) We find that the absorbance edge of a 2 QL film is

$$\omega_{\text{edge}} = \begin{cases} +2(\mu - \varepsilon_L + D_L k_{\text{edge}}^2), & \mu - \varepsilon_L > \frac{\Delta_L}{2} \\ \Delta_L, & -\frac{\Delta_L}{2} < \mu - \varepsilon_L < \frac{\Delta_L}{2} \\ -2(\mu - \varepsilon_L + D_L k_{\text{edge}}^2), & \mu - \varepsilon_L < -\frac{\Delta_L}{2}, \end{cases} \tag{45}$$
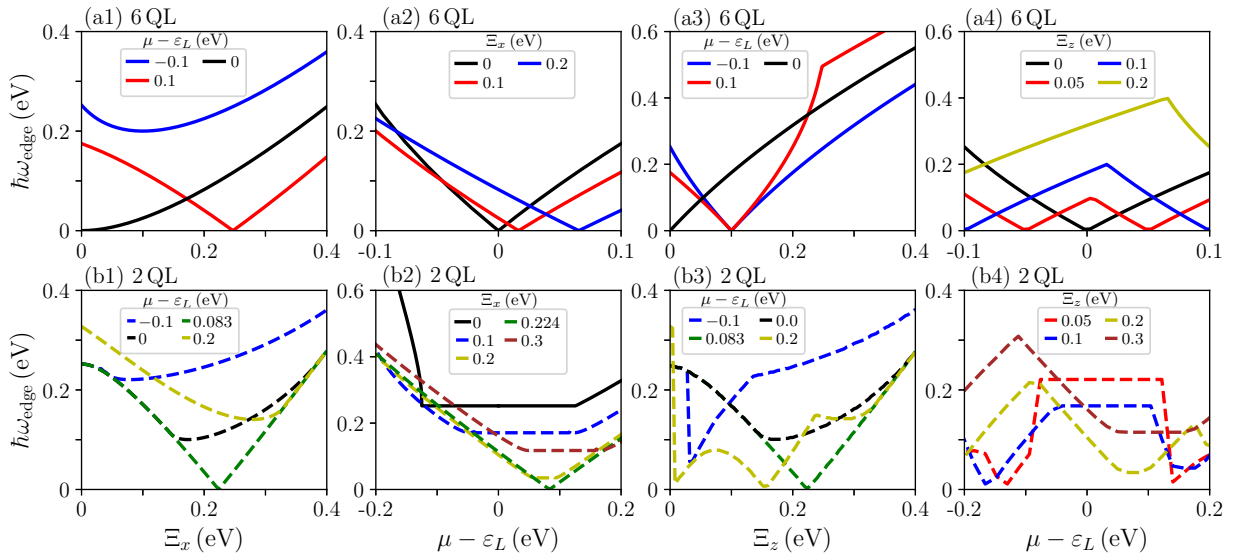
FIG. 6. $\hbar\omega_{\text{edge}}$ of a 6 QL film as a function of (a1) Ξ_x for various $\mu - \varepsilon_L$, (a2) $\mu - \varepsilon_L$ for various Ξ_x, (a3) Ξ_z for various $\mu - \varepsilon_L$, and (a4) $\mu - \varepsilon_L$ for various Ξ_z. Similar plots for a 2 QL film are in (b1)–(b4).

when $\Xi_x = 0$. Here,

$$k_{\text{edge}}^2 = \frac{-\hbar^2 v_{\text{F}}^2 + B_L \Delta_L + 2(\mu - \varepsilon_L)D_L}{2(B_L^2 - D_L^2)} + \frac{\left\{ \hbar^4 v_{\text{F}}^4 + [D_L\Delta_L + 2(\mu - \varepsilon_L)B_L]^2 - 2\hbar^2 v_{\text{F}}^2 [B_L\Delta_L + 2(\mu - \varepsilon_L)D_L] \right\}^{\frac{1}{2}}}{2(B_L^2 - D_L^2)}.$$

The above analytical estimate is shown as a black dotted line in the contour plot in Fig. 2(c1).

(xi) We find that the absorbance edge of 6 QL film is

$$\omega_{\text{edge}} = \begin{cases} \frac{-\hbar v_{\text{F}} + \sqrt{\hbar^2 v_{\text{F}}^2 - 4D_L(\mu - \varepsilon_L - \Xi_z)}}{-D_L/v_{\text{F}}}, & \mu - \varepsilon_L > \Xi_z \\[2mm] \frac{\hbar v_{\text{F}} - \sqrt{\hbar^2 v_{\text{F}}^2 - 4D_L(\mu - \varepsilon_L - \Xi_z)}}{-D_L/v_{\text{F}}}, & \Xi_z > \mu - \varepsilon_L > \frac{-D_L \Xi_z^2}{\hbar^2 v_{\text{F}}^2} \\[2mm] \frac{-\hbar v_{\text{F}} + \sqrt{\hbar^2 v_{\text{F}}^2 - 4D_L(\mu - \varepsilon_L + \Xi_z)}}{-D_L/v_{\text{F}}}, & \frac{-D_L \Xi_z^2}{\hbar^2 v_{\text{F}}^2} > \mu - \varepsilon_L > -\Xi_z \\[2mm] \frac{\hbar v_{\text{F}} - \sqrt{\hbar^2 v_{\text{F}}^2 - 4D_L(\mu - \varepsilon_L + \Xi_z)}}{-D_L/v_{\text{F}}}, & -\Xi_z > \mu - \varepsilon_L, \end{cases} \quad (46)$$

when $\Xi_z \neq 0$. Note that the presence of the term $\mu - \varepsilon_L + \frac{D_L \Xi_z^2}{\hbar^2 v_{\text{F}}^2}$ implies that ω_{edge} is not a function of only $\mu - \varepsilon_L \pm \Xi_z$, but a function of both $\mu - \varepsilon_L$ and Ξ_z. It follows that $\mu - \varepsilon_L$ and Ξ_z differently influence ω_{edge}. The above analytical estimate is shown as a black dotted line in the contour plot in Fig. 5(a1). Naively neglecting the intrinsic electron-hole asymmetry, one finds that $\omega_{\text{edge}} = \frac{2|\mu - \Xi_z|}{\hbar}\Theta(\mu) + \frac{2|\mu + \Xi_z|}{\hbar}\Theta(-\mu)$, which implies that the absorbance edge is an even function of the chemical potential.

(xii) Figure 6 further emphasizes distinct influences of Ξ_x, Ξ_z, and $\mu - \varepsilon_L$ on ω_{edge}. Remarkably, ω_{edge} of a 6 QL and a 2 QL film can be shifted about 0.4 and 0.3 eV, respectively, with the application of moderate electric fields about 0.4 Vnm^{-1}. Moreover, with the chemical potential variations about 0.1 and 0.3 eV, ω_{edge} of a 6 QL and a 2 QL film can be shifted about 0.25 and 0.40 eV, respectively. This wide range of

tunability, 0.3 eV, is of prime importance, considering that TI thin films are expected to be complementary to graphene, transition-metal dichalcogenides, and phosphorene for photon energies below 0.3 eV.

In conclusion, we have presented an effective continuous model for surface states and thin films of TIs subjected to in-plane and out-of-plane static electric fields. We show that the static electric field influences the band structure and the JDOS. Consequently, the absorbance and dichroism spectra strongly depend on both the external electric field and the chemical potential. Regarding the remarkable technological progress in their fabrication [12–14], the experimental demonstration of the electric field tuning of their surface band structure [24], and the advances in the control of their chemical potential [13,35,36], TI thin films are promising for electro-optic modulators and switches. Furthermore, the absorbance and dichroism spectra, and particularly the absorbance edge, can be measured to provide information on the thickness-dependent band gap of the topological surface states as a manifestation of the hybridization phenomenon, the considerable absorbance at the absorbance edge as a signature of the Van Hove singularity in the JDOS, the intrinsic electron-hole asymmetry of surface states, and the robustness against the weak nonmagnetic impurities.

TABLE I. Four possible combinations of ε_+^0 and ε_-^0, and corresponding parameters κ_z and $\kappa_\parallel$.

ε_+^0	ε_-^0	κ_z	$\kappa_\parallel$
Case A	Case A	Real	Real
Case A	Case B	Imaginary	Imaginary
Case B	Case A	Imaginary	Imaginary
Case B	Case B	Real	Real

APPENDIX A: EFFECTIVE HAMILTONIAN

The Hamiltonian can be written as $H = H_0 + \Delta H$, where

$$H_0 = H_{\mathrm{TI}}(\mathbf{k} = 0) = \begin{pmatrix} h_0(A_1) & 0 \\ 0 & h_0(-A_1) \end{pmatrix} \quad \text{(A1)}$$

and

$$h_0(A_1) = \begin{pmatrix} -D_-\partial_z^2 + C + M & -iA_1\partial_z \\ -iA_1\partial_z & -D_+\partial_z^2 + C - M \end{pmatrix}. \quad \text{(A2)}$$

The solutions of $h_0(A_1)\Psi_\uparrow = \varepsilon\Psi_\uparrow$ are $\Psi_{\alpha\beta}^\uparrow e^{\beta\lambda_\alpha z}$, where $\alpha = 1, 2$, $\beta = +, -$, $\Psi_{\alpha\beta}^\uparrow = (D_+\lambda_\alpha^2 - C + M + \varepsilon, -i\beta\lambda_\alpha A_1)^T$, $\lambda_\alpha(\varepsilon) = [\frac{-F(\varepsilon)}{2D_-D_+} + (-1)^{\alpha-1}\frac{\sqrt{G(\varepsilon)}}{2D_-D_+}]^{1/2}$, $D_\pm = D_1 \pm B_1$, $F(\varepsilon) = A_1^2 + D_+(\varepsilon - C - M) + D_-(\varepsilon - C + M)$, and $G(\varepsilon) = F^2(\varepsilon) - 4D_+D_-(\varepsilon - C - M)(\varepsilon - C + M)$. Writing the general solution as a linear combination of four independent eigenvectors, $\Psi_\uparrow = \sum_{\alpha=1,2}\sum_{\beta=\pm} C_{\alpha\beta}\Psi_{\alpha\beta}^\uparrow e^{\beta\lambda_\alpha z}$, and imposing the boundary conditions $\Psi_\uparrow(z = \pm\frac{L}{2}) = 0$ leads to two transcendental equations for two eigenenergies ε_+^0 and ε_-^0. The eigenfunctions corresponding to ε_+^0 and ε_-^0 are

$$\varphi(A_1) = \Psi_\uparrow^+ = c_+\begin{pmatrix} -D_+\eta_1^+ f_+^+ \\ iA_1 f_+^+ \end{pmatrix},$$

$$\chi(A_1) = \Psi_\uparrow^- = c_-\begin{pmatrix} -D_+\eta_2^- f_-^- \\ iA_1 f_-^- \end{pmatrix}, \quad \text{(A3)}$$

respectively. c_+ and c_- are normalization factors, and

$$f_+^\pm(z) = \frac{\cosh(\lambda_1 z)}{\cosh\left(\frac{\lambda_1 L}{2}\right)} - \frac{\cosh(\lambda_2 z)}{\cosh\left(\frac{\lambda_2 L}{2}\right)}\bigg|_{\varepsilon=\varepsilon_\pm^0},$$

$$f_-^\pm(z) = \frac{\sinh(\lambda_1 z)}{\sinh\left(\frac{\lambda_1 L}{2}\right)} - \frac{\sinh(\lambda_2 z)}{\sinh\left(\frac{\lambda_2 L}{2}\right)}\bigg|_{\varepsilon=\varepsilon_\pm^0},$$

$$\eta_1^\pm = \frac{\lambda_1^2 - \lambda_2^2}{\lambda_1 \cot\left(\frac{\lambda_1 L}{2}\right) - \lambda_2 \cot\left(\frac{\lambda_2 L}{2}\right)}\bigg|_{\varepsilon=\varepsilon_\pm^0},$$

$$\eta_2^\pm = \frac{\lambda_1^2 - \lambda_2^2}{\lambda_1 \tan\left(\frac{\lambda_1 L}{2}\right) - \lambda_2 \tan\left(\frac{\lambda_2 L}{2}\right)}\bigg|_{\varepsilon=\varepsilon_\pm^0}. \quad \text{(A4)}$$

The eigenenergies and eigenfunctions of the lower block of H_0 can be similarly obtained. The four eigenstates of H_0 are $\Phi_1 = \binom{\varphi(+A_1)}{0}$, $\Phi_2 = \binom{\chi(+A_1)}{0}$, $\Phi_3 = \binom{0}{\varphi(-A_1)}$, and $\Phi_4 = \binom{0}{\chi(-A_1)}$.

To obtain an effective Hamiltonian for a TI thin film under a static electric field, we project H into the surface states Φ_1, Φ_4, Φ_2, and Φ_3, and exclude the contribution of the bulk states. Indeed, $H^{\mathrm{eff}} = H_{\mathrm{TI}}^{\mathrm{eff}} + H_{\mathrm{E}}^{\mathrm{eff}}$, where

$$H_{\mathrm{TI}}^{\mathrm{eff}} = \int_{-\frac{L}{2}}^{\frac{L}{2}} dz[\Phi_1, \Phi_4, \Phi_2, \Phi_3]^* H_{\mathrm{TI}}[\Phi_1, \Phi_4, \Phi_2, \Phi_3],$$

$$H_{\mathrm{E}}^{\mathrm{eff}} = \int_{-\frac{L}{2}}^{\frac{L}{2}} dz[\Phi_1, \Phi_4, \Phi_2, \Phi_3]^* H_{\mathrm{E}}[\Phi_1, \Phi_4, \Phi_2, \Phi_3]. \quad \text{(A5)}$$

We find that two parameters,

$$\kappa_z = \langle\varphi(A_1)|\,\sigma_y\,|\chi(+A_1)\rangle, \quad \kappa_\parallel = \langle\varphi(A_1)|\,\sigma_y\,|\chi(-A_1)\rangle, \quad \text{(A6)}$$

are sufficient to express the effective Hamiltonian $H_{\mathrm{E}}^{\mathrm{eff}}$ [see Eq. (3)]. The parameters $\varepsilon_L = (\varepsilon_+^0 + \varepsilon_-^0)/2$, $\Delta_L = \varepsilon_+^0 - \varepsilon_-^0$,

$$B_L = B_2[\langle\varphi(A_1)|\,\sigma_z\,|\varphi(A_1)\rangle - \langle\chi(A_1)|\,\sigma_z\,|\chi(A_1)\rangle]/2,$$

$$D_L = B_2[\langle\varphi(A_1)|\,\sigma_z\,|\varphi(A_1)\rangle + \langle\chi(A_1)|\,\sigma_z\,|\chi(A_1)\rangle]/2 - D_2,$$

are of use to express the effective Hamiltonian $H_{\mathrm{TI}}^{\mathrm{eff}}$ [20].

We remind the reader that $D_+D_- < 0$ for the Bi$_2$Se$_3$ TI. If $G(\varepsilon) < 0$, then $\lambda_1(\varepsilon) = \lambda_2^*(\varepsilon)$ and it follows that $f_\pm^\pm(z)$ are imaginary and $\eta_{1,2}^\pm$ are real (case A). If $G(\varepsilon) > 0$ and $\sqrt{G(\varepsilon)} > F(\varepsilon)$, then $\lambda_1(\varepsilon)$ is imaginary and $\lambda_2(\varepsilon)$ is real. If $G(\varepsilon) > 0$ and $F(\varepsilon) > 0$ but $\sqrt{G(\varepsilon)} < F(\varepsilon)$, then both $\lambda_1(\varepsilon)$ and $\lambda_2(\varepsilon)$ are real. It follows that both $f_\pm^\pm(z)$ and $\eta_{1,2}^\pm$ are real (case B). It is clear that according to the values of ε_+^0 and ε_-^0, four different cases may happen. However, κ_z and $\kappa_\parallel$ are either both real or both imaginary (see Table I). We also find that $\langle\varphi(+A_1)|\,\sigma_x\,|\chi(-A_1)\rangle = i\kappa_z$, which shows that $A_L = A_2\langle\varphi(A_1)|\,\sigma_x\,|\chi(-A_1)\rangle = iA_2\kappa_z$ is real (imaginary) when κ_z and $\kappa_\parallel$ are imaginary (real).

APPENDIX B: WAVE VECTOR k_{gap}

To minimize the function $\varsigma_1(\mathbf{k}, \Xi_x)$, we encounter a cubic equation of the type $k_{\mathrm{gap}}^3 + a_1 k_{\mathrm{gap}} + a_0 = 0$. Here, $a_0^2/4 + a_1^3/27 > 0$, and thus the only real root of the cubic equation is

$$k_{\mathrm{gap}} = \left[-a_0/2 + \sqrt{a_0^2/4 + a_1^3/27}\right]^{1/3}$$

$$+ \left[-a_0/2 - \sqrt{a_0^2/4 + a_1^3/27}\right]^{1/3}. \quad \text{(B1)}$$

[1] B. E. A. Saleh and M. C. Teich, *Fundamentals of Photonics* (Wiley, New York, 2007).

[2] S. L. Chuang, *Physics of Photonic Devices* (Wiley, Hoboken, NJ, 2012).

[3] F. Bonaccorso, Z. Sun, T. Hasan, and A. C. Ferrari, Graphene photonics and optoelectronics, Nat. Photon. **4**, 611 (2010).

[4] Z. Sun, A. Martinez, and F. Wang, Optical modulators with 2D layered materials, Nat. Photon. **10**, 227 (2016).

[5] X. Zhou, X. Hu, J. Yu, S. Liu, Z. Shu, Q. Zhang, H. Li, Y. Ma, H. Xu, and T. Zhai, 2D layered material-based van der Waals heterostructures for optoelectronics, Adv. Funct. Mater. **28**, 1706587 (2018).

[6] R. R. Nair, P. Blake, A. N. Grigorenko, K. S. Novoselov, T. J. Booth, T. Stauber, N. M. R. Peres, and A. K. Geim, Fine structure constant defines visual transparency of graphene, Science **320**, 1308 (2008).

[7] K.-F. Mak, M. Y. Sfeir, Y. Wu, C.-H. Lui, J. A. Misewich, and T. F. Heinz, Measurement of the Optical Conductivity of Graphene, Phys. Rev. Lett. **101**, 196405 (2008).

[8] A. Rogalski, Quantum well photoconductors in infrared detector technology, J. Appl. Phys. **93**, 4355 (2003).

[9] X. Zhang, J. Wang, and S.-C. Zhang, Topological insulators for high-performance terahertz to infrared applications, Phys. Rev. B **82**, 245107 (2010).

[10] M. Z. Hasan and C. L. Kane, Colloquium: Topological insulators, Rev. Mod. Phys. **82**, 3045 (2010).

[11] X.-L. Qi and S.-C. Zhang, Topological insulators and superconductors, Rev. Mod. Phys. **83**, 1057 (2011).

[12] G. Zhang, H. Qin, J. Teng, J. Guo, Q. Guo, X. Dai, Z. Fang, and K. Wu, Quintuple-layer epitaxy of thin films of topological insulator Bi_2Se_3, Appl. Phys. Lett. **95**, 053114 (2009).

[13] D. Kong, W. Dang, J. J. Cha, H. Li, S. Meister, H. Peng, Z. Liu, and Y. Cui, Few-layer nanoplates of Bi_2Se_3 and Bi_2Te_3 with highly tunable chemical potential, Nano Lett. **10**, 2245 (2010).

[14] D. Teweldebrhan, V. Goyal, and A. A. Balandin, Exfoliation and characterization of bismuth telluride atomic quintuples and quasi-two-dimensional crystals, Nano Lett. **10**, 1209 (2010).

[15] H. Zhang, C.-X. Liu, X.-L. Qi, X. Dai, Z. Fang, and S.-C. Zhang, Topological insulators in Bi_2Se_3, Bi_2Te_3 and Sb_2Te_3 with a single Dirac cone on the surface, Nat. Phys. **5**, 438 (2009).

[16] Y. Xia, D. Qian, D. Hsieh, L. Wray, A. Pal, H. Lin, A. Bansil, D. Grauer, Y. S. Hor, R. J. Cava, and M. Z. Hasan, Observation of a large-gap topological-insulator class with a single Dirac cone on the surface, Nat. Phys. **5**, 398 (2009).

[17] Y. L. Chen, J. G. Analytis, J.-H. Chu, Z. K. Liu, S.-K. Mo, X. L. Qi, H. J. Zhang, D. H. Lu, X. Dai, Z. Fang, S. C. Zhang, I. R. Fisher, Z. Hussain, and Z.-X. Shen, Experimental realization of a three-dimensional topological insulator, Bi_2Te_3, Science **325**, 178 (2009).

[18] T. Zhang, P. Cheng, X. Chen, J.-F. Jia, X. Ma, K. He, L. Wang, H. Zhang, X. Dai, Z. Fang, X. Xie, and Q.-K. Xue, Experimental Demonstration of Topological Surface States Protected by Time-Reversal Symmetry, Phys. Rev. Lett. **103**, 266803 (2009).

[19] Y. Zhang, K. He, C. Z. Chang, C. L. Song, L. L. Wang, X. Chen, J. F. Jia, Z. Fang, X. Dai, W. Y. Shan, S. Q. Shen, Q. Niu, X. L. Qi, S. C. Zhang, X. C. Ma, and Q. K. Xue, Crossover of the three-dimensional topological insulator Bi_2Se_3 to the two-dimensional limit, Nat. Phys. **6**, 584 (2010).

[20] W.-Y. Shan, H.-Z. Lu, and S.-Q. Shen, Effective continuous model for surface states and thin films of three-dimensional topological insulators, New J. Phys. **12**, 043048 (2010).

[21] H.-Z. Lu, W.-Y. Shan, W. Yao, Q. Niu, and S.-Q. Shen, Massive Dirac fermions and spin physics in an ultrathin film of topological insulator, Phys. Rev. B **81**, 115407 (2010).

[22] M. Kim, C. H. Kim, H.-S. Kim, and J. Ihm, Topological quantum phase transitions driven by external electric fields in Sb_2Te_3 thin films, Proc. Natl. Acad. Sci. USA **109**, 671 (2012).

[23] Y. Jiang, Y. Wang, M. Chen, Z. Li, C. Song, K. He, L. Wang, X. Chen, X. Ma, and Q.-K. Xue, Landau Quantization and the

[24] Thickness Limit of Topological Insulator Thin Films of Sb_2Te_3, Phys. Rev. Lett. **108**, 016401 (2012).

[24] T. Zhang, J. Ha, N. Levy, Y. Kuk, and J. Stroscio, Electric-Field Tuning of the Surface Band Structure of Topological Insulator Sb_2Te_3 Thin Films, Phys. Rev. Lett. **111**, 056803 (2013).

[25] M. Lasia and L. Brey, Optical properties of magnetically doped ultrathin topological insulator slabs, Phys. Rev. B **90**, 075417 (2014).

[26] F. Parhizgar, A. G. Moghaddam, and R. Asgari, Optical response and activity of ultrathin films of topological insulators, Phys. Rev. B **92**, 045429 (2015).

[27] L. Zhao, J. Wang, J. Liu, Y. Xu, B.-L. Gu, Q.-K. Xue, and W. Duan, Electronic analog of chiral metamaterial: Helicity-resolved filtering and focusing of Dirac fermions in thin films of topological materials, Phys. Rev. B **92**, 041408(R) (2015).

[28] M. Shiranzaei, F. Parhizgar, J. Fransson, and H. Cheraghchi, Impurity scattering on the surface of topological-insulator thin films, Phys. Rev. B **95**, 235429 (2017).

[29] M. R. Brems, J. Paaske, A. M. Lunde, and M. Willatzen, Strain-enhanced optical absorbance of topological insulator films, Phys. Rev. B **97**, 081402(R) (2018).

[30] Y. Xu, G. Jiang, I. Miotkowski, R. R. Biswas, and Y. P. Chen, Tuning Insulator-Semimetal Transitions in 3D Topological Insulator thin Films by Intersurface Hybridization and In-Plane Magnetic Fields, Phys. Rev. Lett. **123**, 207701 (2019).

[31] Y. Jiang, M. M. Asmar, X. Han, M. Ozerov, D. Smirnov, M. Salehi, S. Oh, Z. Jiang, W.-K. Tse, and L. Wu, Electron-hole asymmetry of surface states in topological insulator Sb_2Te_3 thin films revealed by magneto-infrared spectroscopy, Nano Lett. **20**, 4588 (2020).

[32] J. Wang, H. Mabuchi, and X.-L. Qi, Calculation of divergent photon absorption in ultrathin films of a topological insulator, Phys. Rev. B **88**, 195127 (2013).

[33] D. West and S. B. Zhang, Thin-film topological insulators for continuously tunable terahertz absorption, Appl. Phys. Lett. **112**, 091601 (2018).

[34] M. R. Brems, J. Paaske, A. M. Lunde, and M. Willatzen, Symmetry analysis of strain, electric and magnetic fields in the Bi_2Se_3-class of topological insulators, New J. Phys. **20**, 053041 (2018).

[35] J. Chen, H. J. Qin, F. Yang, J. Liu, T. Guan, F. M. Qu, G. H. Zhang, J. R. Shi, X. C. Xie, C. L. Yang, K. H. Wu, Y. Q. Li, and L. Lu, Gate-Voltage Control of Chemical Potential and Weak Antilocalization in Bi_2Se_3, Phys. Rev. Lett. **105**, 176602 (2010).

[36] D. Kim, S. Cho, N. P. Butch, P. Syers, K. Kirshenbaum, S. Adam, J. Paglione, and M. S. Fuhrer, Surface conduction of topological Dirac electrons in bulk insulating Bi_2Se_3, Nat. Phys. **8**, 459 (2012).

[37] G. Landolt, S. Schreyeck, S. V. Eremeev, B. Slomski, S. Muff, J. Osterwalder, E. V. Chulkov, C. Gould, G. Karczewski, K. Brunner, H. Buhmann, L. W. Molenkamp, and J. H. Dil, Spin Texture of Bi_2Se_3 Thin Films in the Quantum Tunneling Limit, Phys. Rev. Lett. **112**, 057601 (2014).

[38] P. Tsipas, E. Xenogiannopoulou, S. Kassavetis, D. Tsoutsou, E. Golias, C. Bazioti, G. P. Dimitrakopulos, P. Komninou, H. Liang, M. Caymax, and A. Dimoulas, Observation of surface Dirac cone in high-quality ultrathin epitaxial Bi_2Se_3 topological insulator on AlN (0001) dielectric, ACS Nano **8**, 6614 (2014).